Supporting Information

2D WO_3 nanosheets for high-performance electrochromic-supercapacitor

Shen Wang[a], Hongbo Xu[a] , Jiupeng Zhao[a], Yao Li[b]*+*

[a]School of Chemistry and Chemical Engineering, Harbin Institute of Technology, Harbin, 150001, PR China.

[b]Center for Composite Materials and Structure, Harbin Institute of Technology, Harbin 150001, PR China.

**Corresponding author: yaoli@hit.edu.cn; jpzhao@hit.edu.cn.*

Electronic Supplementary Information Index

Figure S5. XRD patterns of WO_3 nanosheets array/FTO percussor with different solvothermal treatment time.

Figure S6. Schematic illustrating of the forming process of WO_3 nanosheets array/FTO.

Figure S7. CV curves at 20 mV s^{-1} and in situ corresponding spectral changes of WO_3 nanosheets array/FTO dual-functional electrode: (a1, a2 and a3) WO_3 /FTO-0, (b1, b2 and b3) WO_3 NSHs/FTO-0.4, (c1, c2 and c3) WO_3 NSHs/FTO, (d1, d2 and d3) WO_3 NSHs/FTO-0.6.

Figure S8. CV curves and in situ corresponding spectral changes of WO_3 nanosheets array/FTO dual-functional electrode at different scan rates: (a1 and a2) 5 mV s^{-1}, (b1 and b2) 10 mV s^{-1}, (c1 and c2) 20 mV s^{-1}, (d1 and d2) 50 mV s^{-1}, (e1 and e2) 60 mV s^{-1}, (f1 and f2) 80 mV s^{-1}, (g1 and g2) 100 mV s^{-1}.

Figure S9. Full transmittance spectra of the WO_3 nanosheets array/FTO electrode during the positive scan of 5 mV s^{-1}.

Figure S10. Areal specific capacitance and corresponding optical modulation at 1000 nm at different scan rates.

Figure S11. The determination of the b-value at anodic peak regimes.

Figure S12. The CP curves and in situ corresponding spectral changes for the WO_3 nanosheets array/FTO electrode at different current densities: (a1 and a2) 3 mA cm^{-2}, (b1 and b2) 4 mA cm^{-2}, (c1 and c2) 5mA cm^{-2}, (d1 and d2) 6 mA cm^{-2}, (e1 and e2) 7 mA cm^{-2}.

Figure S13. (a) The relationship between transmittance change profile at 1000 nm

and charge/discharge curve at 3 mA cm^{-2}, (b) Full transmittance spectra of the WO_3 nanosheets array/FTO electrode during the charge process at 3 mA cm^{-2}, (c) Influence of different current densities on the areal specific capacitance and the transmittance change at 1000 nm of the WO_3 nanosheets array/FTO electrode.

Figure S14. (a), (b) and (c) In-situ corresponding spectral changes at a scan rate of 40 mV s^{-1} after different CV cycles, (d) Nyquist plots of the WO_3 nanosheets array/FTO electrode before and after 10000 cycles.

Figure S15. SEM images of the WO_3 WO_3 nanosheets array/FTO electrode after 10000 cycles.

Figure S16. The corresponding 2D contour maps of (420) and (404) peaks of the WO_3 nanosheets array/FTO electrode.

Figure S17. Ex-situ XPS spectra of W 4f at different potential states of WO_3 nanosheets array/FTO electrode.

Figure S18. (a) and (b) SEM images, (c) XRD pattern of the V_2O_5 /FTO, (d) CV curves of the electrode at different scan rates, (e) CP curves of full cell at different current densities from 1 to 4 mA cm^{-2}, (f) The areal specific capacitance at different scan rates.

Figure S19. (a) Schematic illustration of the assembly of an electrochromic supercapacitor, (b) CV curves of WO_3 NSHs/FTO and V_2O_5 /FTO electrode tested in three-electrode system at the scan rate of 20 mV s^{-1}, (c) CV curves of the device at different potential windows during the scan rate of 20 mV s^{-1}, (d) CV curves of the device at different scan rates.

Table S1 Comparison of the electrochromic and energy storage performance between WO_3 in this work and before.

Table S2. The digital photos of the electrochromic supercapacitor at different capacity status and corresponding (L a b) values.

Experimental section

1.1 Preparation V_2O_5 /FTO

V_2O_5 /FTO was prepared by a simple solvothermal method. In short, 0.7 g V_2O_5, 0.9 g 1-hexadecylamine and 0.4 g Poly(ethylene glycol)-block-poly(propylene glycol)-block-poly(ethylene glycol) were dissolved into 60 mL mixed solution (40 mL isopropanol and 20 mL deionized water) and continuous stirring 48 h. Then the above solution was transferred into a 100 mL Teflon-lined autoclave with the treated FTO and maintained at 160 ^oC for 72 h. After cooling down to room temperature naturally, the FTO glass was taken out and washed with deionized water and ethanol several times before drying in a vacuum oven at 60 ^oC for 12 h. Finally, the as-prepared films were annealed at 400 ^oC for 2 h in air.

1.2 The assembled electrochromic supercapacitor (ESC) full cell

We used the V_2O_5 /FTO (2 cm × 4 cm) as the positive electrode, WO_3 nanosheets array/FTO (2 cm × 4 cm) as the negative electrode and 1 mol L^{-1} $AlCl_3$ aqueous solution as the electrolyte to constructed a ESC device (1.8 cm × 3 cm). Firstly, the positive and negative electrode are separated by transparent tape, then a small hole is reserved, and the remaining part is encapsulated with UV-curable adhesive. Finally, the electrolyte is injected into the gap between the positive and negative electrodes

with a syringe and sealed with UV-curable adhesive.

1.3 Characterization

The crystalline structure of WO_3 NSHs/FTO was tested by X-ray diffraction (XRD) patterns on a Bruker D8 Advance X-ray diffractometer using Cu K (λ = 1.5418 Å) as the source at a scanning rate of 5° min^{-1} with a 2θ range of 5~80°. Thermal gravimetric analysis (TGA) was characterized in the air from 20~800 °C at a heating rate of 5 °C min^{-1} by a Shimadzu DTG-60H. The Raman spectra were conducted with a 532 nm laser source (LabRAM HR Evolution). The Brunauer-Emmett-Teller (BET) surface specific surface area and the pore size distribution were measured using a Micromeritics ASAP 2020 system. The microstructure of WO_3 NSHs were studied by field emission scanning electron microscope (FESEM, ZISS SUPRA55) and transmission electron microscopy (FETEM, Tecnai G2 F30, 200 kV). X-ray photoelectron spectroscopy (XPS, Thermo Scientific ESCAlab 250Xi photoelectron spectrometer) was used to study the chemical composition and elemental valence.

Electrochemical Measurements

The electrochemical and optical property of a bifunctional electrode were synchronously tested by combining the Chen Hua CHI660E workstation and the VIS-NIR fiber optic spectrometer (MAYA 2000-Pro, Ocean Optics, 200 nm~1100 nm). The working electrode, the counter electrode, and the reference electrode were WO_3 nanosheets array/FTO, Pt sheet and Ag/AgCl electrode, respectively. The bifunctional properties of the electrodes were characterized by integrating the energy storage

testing (cyclic voltammetry (CV), electrochemical impedance spectroscopy (EIS), chronopotentiometry (CP) and the optical performance testing in 1 mol L^{-1} $AlCl_3$ aqueous solution.

In the three-electrode configuration system, an areal capacitance C_s (mF cm^{-2}) of the WO_3 nanosheets array/FTO electrode was calculated from the CV curves depend on the following equation[1, 2]:

$$C_s = \frac{1}{\nu A \Delta V} \oint I(V) dV \quad (1)$$

where A is the effective area of the single electrode (WO_3 nanosheets array/FTO electrode has an active electrode area of roughly 0.9 cm × 2 cm), ν (V s^{-1}) is the potential scan rate, and ΔV (V) is the window.

An areal capacitance C_s (mF cm^{-2}) of the WO_3 nanosheets array/FTO electrode was gained from chronopotentiometry curves according to the following equation[3]:

$$C_s = \frac{2I}{A \Delta V} \int V dt \quad (2)$$

where I is the discharge current (A), A is the area of the electrode (cm^2), ΔV (V) was the potential window, and $\int V dt$ is the area under the discharge curve.

An area capacitance C_{ESC} of the device was calculated from the chronopotentiometry curves[4, 5]

$$C_{ESC} = \frac{I}{A \Delta V} \int V dt \quad (3)$$

where I is the discharge current (A), A is the total area of the device (cm^2) (The ESC device has an active electrode area of roughly 0.7 cm × 2 cm), ΔV (V) was the running potential window of the ESC device, and $\int Vdt$ was the area under the discharge curve.

The energy density (E) and power density(P) of the asymmetrical supercapacitor were calculated according to the following equations[1, 2, 4, 5]:

$$E = C_{ESC} \times V^2 \tag{4}$$

$$P = E/\Delta t \tag{5}$$

where C_{ESC} is the specific capacitance Δt is the discharge time, and V is the voltage window of the as-assembled asymmetric supercapacitor.

In-situ electrochemical measurements were carried out in a polytetrafluoroethylene (PTFE) electrochemical cell[6] including WO_3 nanosheets array/FTO, platinum plate, and Ag/AgCl electrode with 1 mol L^{-1} $AlCl_3$ solution as the electrolyte. In-situ XRD characterizations of WO_3 nanosheets array/FTO were characterized at a scan rate of 0.5 mV s^{-1} with the voltage range of from -0.6 to 0.8 V (vs Ag/AgCl). GSAS-II software was used to explore the evolution of crystalline structure within 2θ region (5° ~ 73°) during the charge/discharge process.

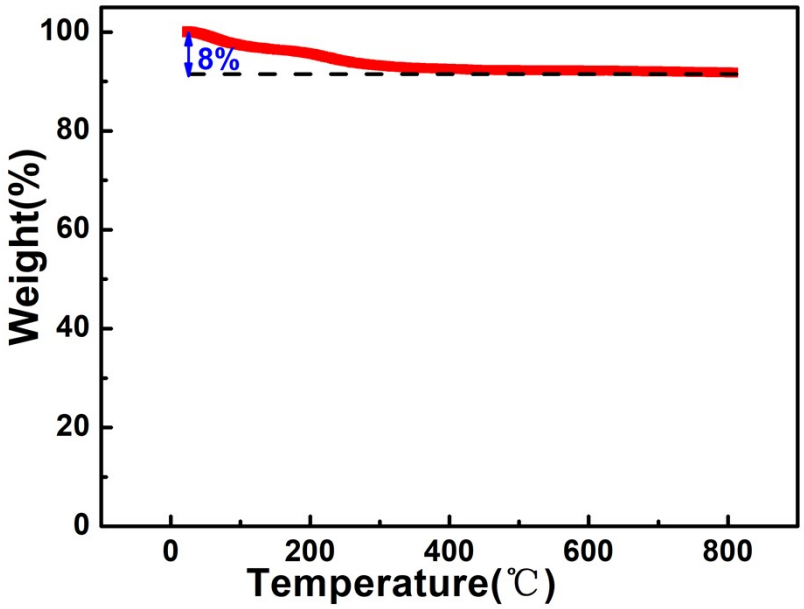

Figure. S1. Thermal gravimetric curve of the WO_3 nanosheets precursor powder at a heating rate of 5 °C min^{-1} in the air.

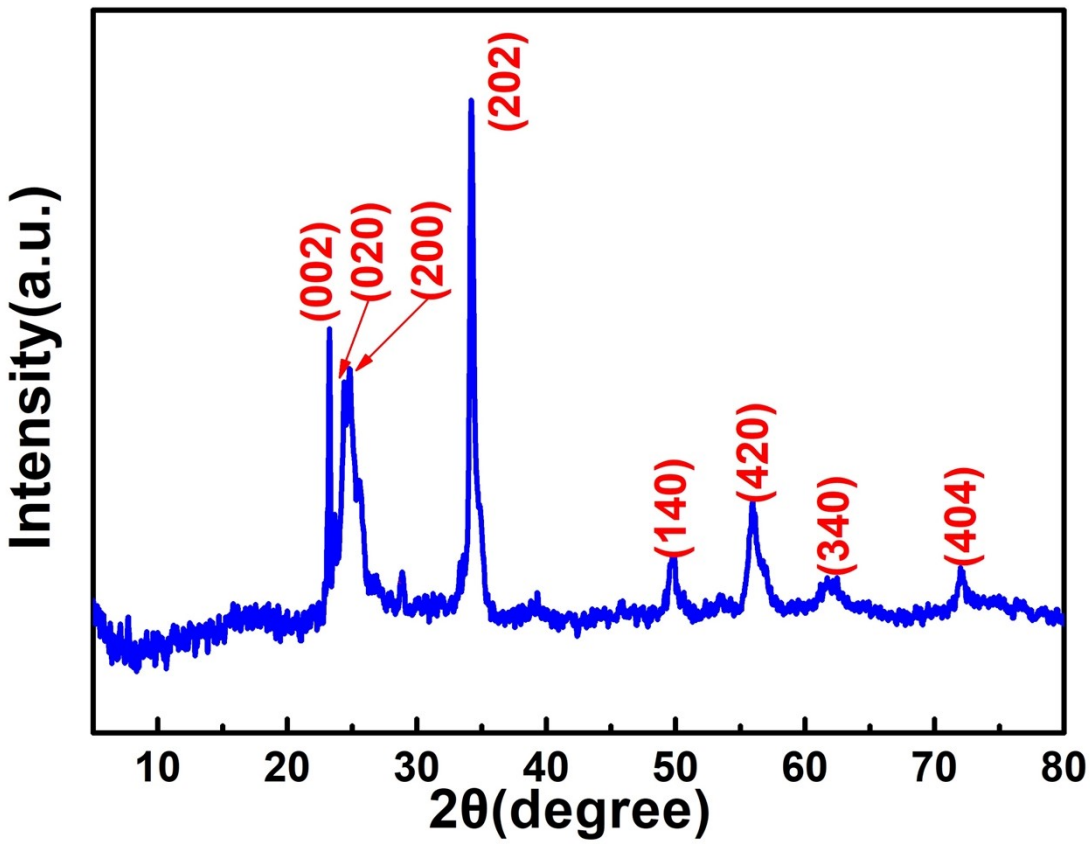

Figure S2. XRD patterns of the WO_3 nanosheets powder.

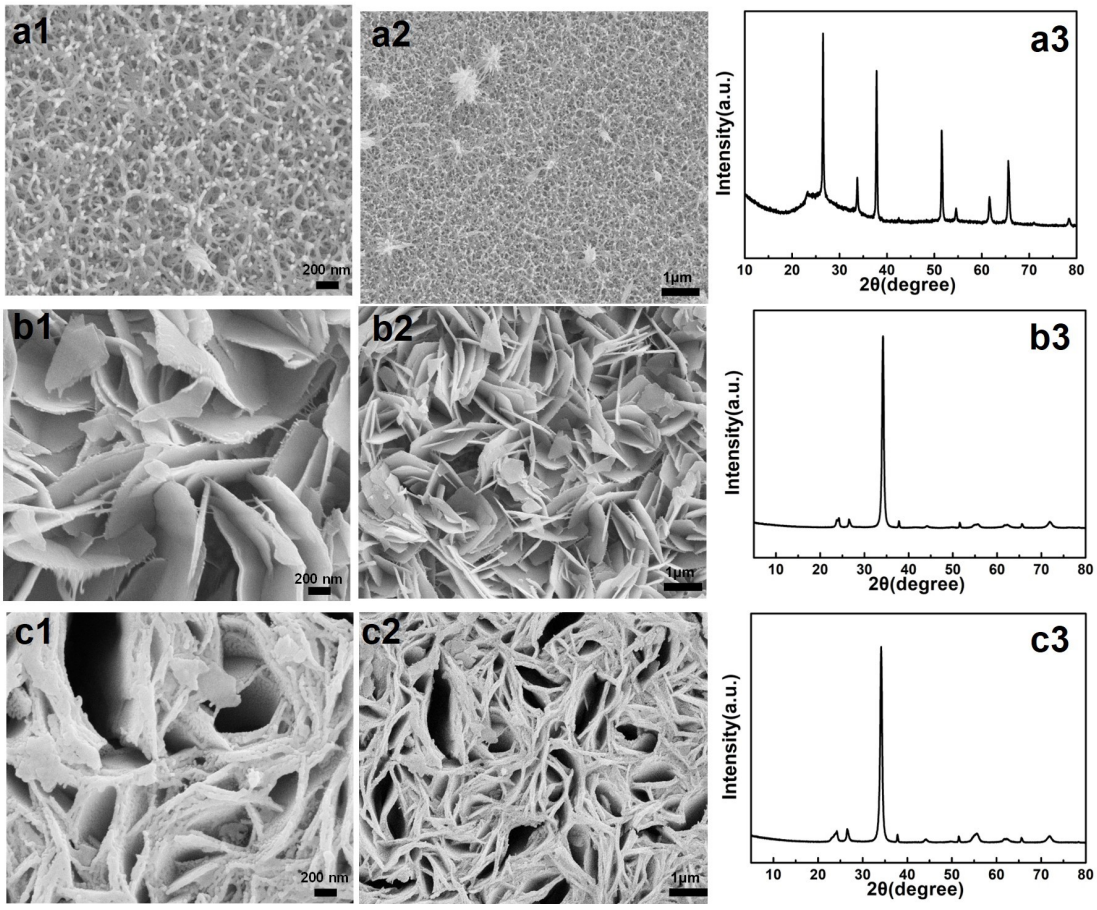

Figure S3. SEM image and XRD spectrum of the WO_3 /FTO samples synthesized under the various amount of P131347: (a1, a2, a3) WO_3 /FTO-0, (b1, b2, b3) WO_3 NSHs/FTO-0.4, (c1, c2, c3) WO_3 NSHs/FTO -0.6.

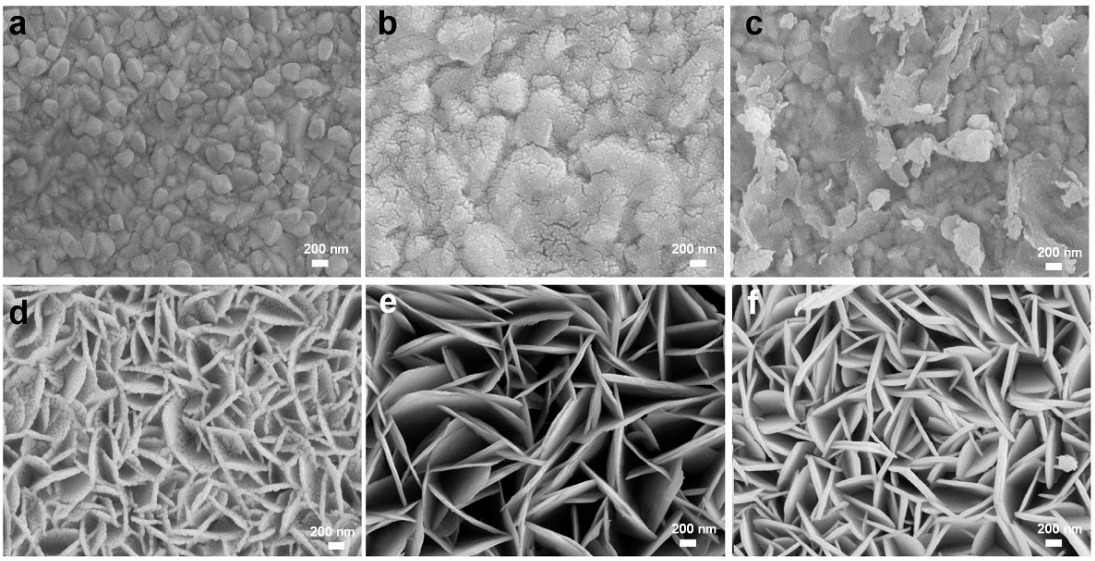

Figure S4. SEM images of WO_3 nanosheets array/FTO percussor with different solvothermal treatment time: (a) 0 h, (b) 1 h, (c) 2 h, (d) 4 h, (e) 6 h, (f) 10 h.

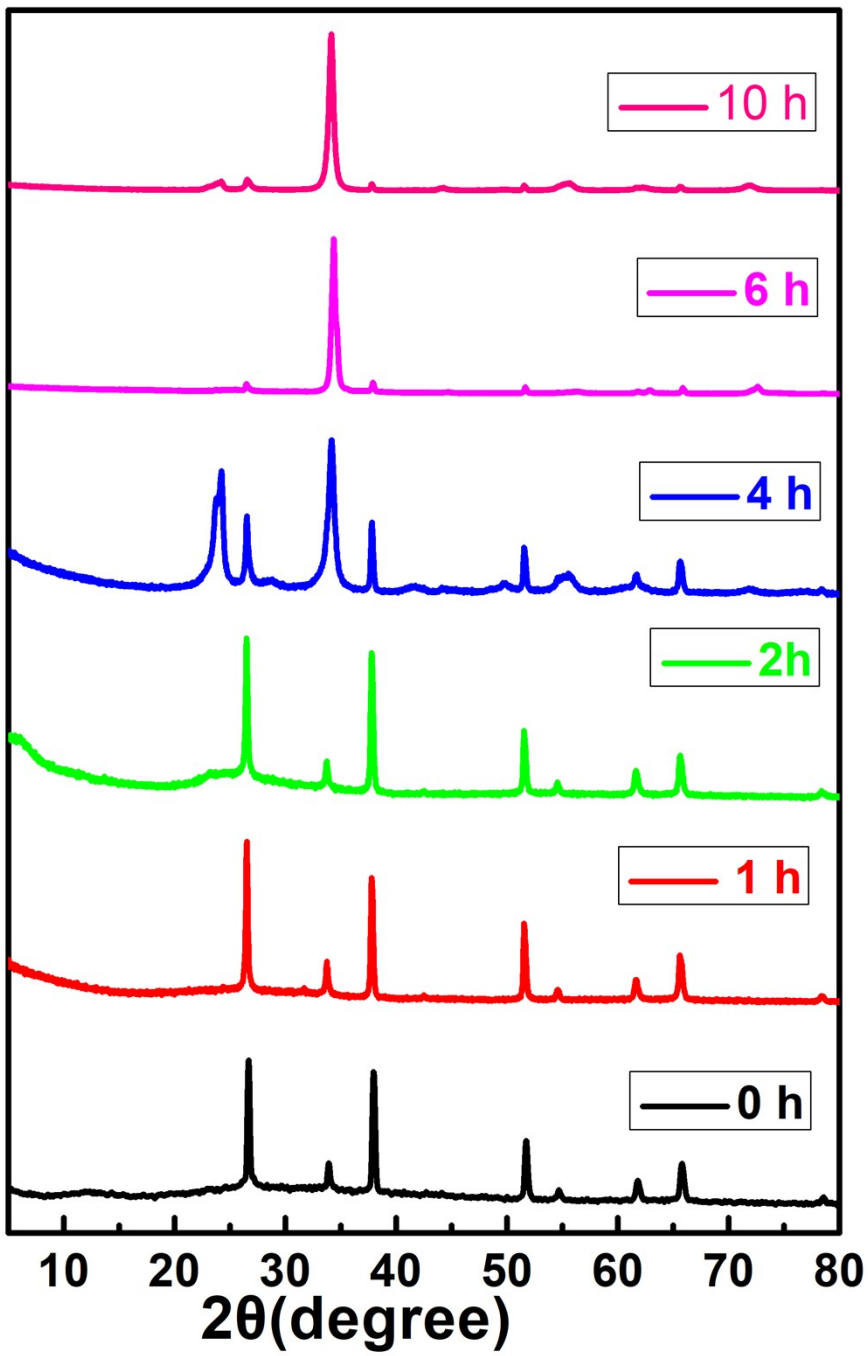

Figure S5. XRD patterns of WO_3 nanosheets array/FTO percussor with different solvothermal treatment time.

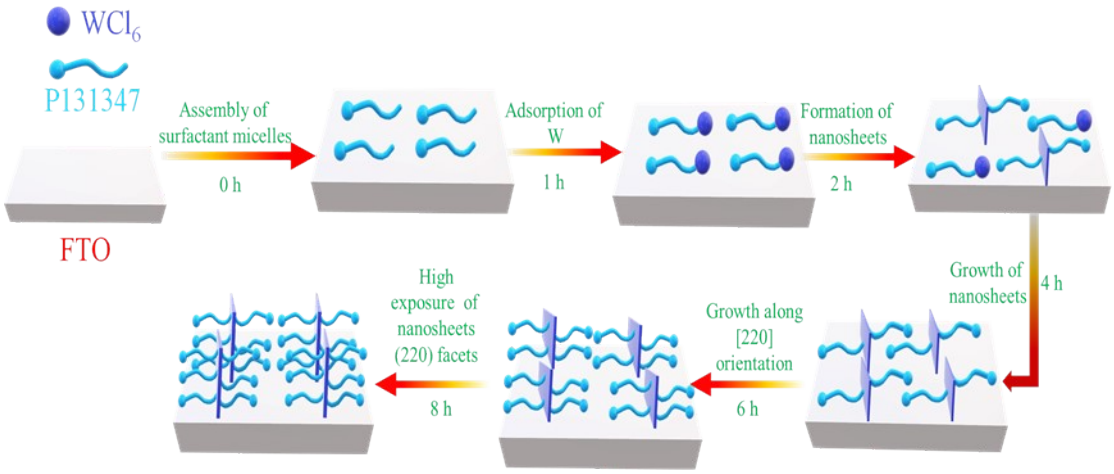

Figure S6. Schematic illustrating of the forming process of WO_3 nanosheets array/FTO.

To study the formation process of WO_3 NSHs/FTO, the time-dependent tests were designed. When the reaction time increased to 1 h, the growth of WO_3 nanoparticles on FTO could be observed (Figure S4 b, Supporting Information), contrast to bare FTO (Figure S4a, Supporting Information). After 2 h, some WO_3 nanosheets began to grow on FTO (Figure S4c, Supporting Information). With the reaction time lengthening to 4 h, many aligned WO_3 nanosheets array successfully assembled on the FTO substrate (Figure S4d, Supporting Information). With the extension of reaction time to 6 h, geometrical dimension of the aligned WO_3 nanosheet sharp increased (Figure S4e, Supporting Information). When the reaction time extended to 10 h, the agglomeration of the adjacent nanosheets occurs (Figure S4f, Supporting Information), which is not conducive to the electrolyte penetration and the exposure of electroactive sites. This indicated that the optimal reaction time was 8 h. From Figure S5 (Supporting Information), XRD patterns of the samples with different reaction time, the diffraction peaks of the two precursors within 2 h show a small broadening peak between 20° and 25° after deducting the diffraction peaks of the blank FTO, which is derived from the obtained amorphous WO_3 and the amount of WO_3 adhered to FTO is relatively low. This result is consistent with the SEM images of the precursors at 1 h and 2 h. When the reaction time increased to 4 h, the XRD peaks belonging to monoclinic WO_3 became stronger, due to improving the crystallinity and loading of WO_3. When the reaction time exceeds 6 h, the peak

intensity of (202) lattice plane is stronger than that of other peaks, which illustrates WO_3 nanosheets with high-orientated (101) facets directionally self-assemble on FTO. This is because the polar groups of P131347 prefer to be adsorbed on the (202) crystal plane to facilitate their exposure. Besides, on the basis of the previous literature[7, 8], ethanol can be used as a co-surfactant, which is helpful to the formation of stable WO_3 nanosheets. In brief, the successful construct of WO_3 NSHs/FTO should be from the synergic effect of reaction time, P131347, and ethanol. Based on the above discussion, a possible growth mechanism of the WO_3 NSHs/FTO with high-orientated (101) facets be deduced (Figure S6, Supporting Information). At the beginning of the experiment, the laminar micelles of P131347 arrays would self-assembly on FTO and adsorb tungsten complex. Secondly, the adsorbed tungsten complex converted into WO_3 nanoparticles and grown on FTO. Then, a little amount of WO_3 nanosheets began to grow vertically on FTO based on the nanoparticles on the substrate as the seed and the lamellar micelles of P131347. With the extension of reaction time, lots of vertical WO_3 nanosheets self-assembled on the FTO substrate, and P131347 adsorbed on the (202) plane reduce the growth rate along this orientation. Subsequently, WO_3 nanosheets array continued to grow along the vertical FTO direction, and the crystallization degree of (202) peak increase. Finally, the WO_3 NSHs/FTO with high-orientated (101) facets were synthetized after the removal of adsorptive P131347.

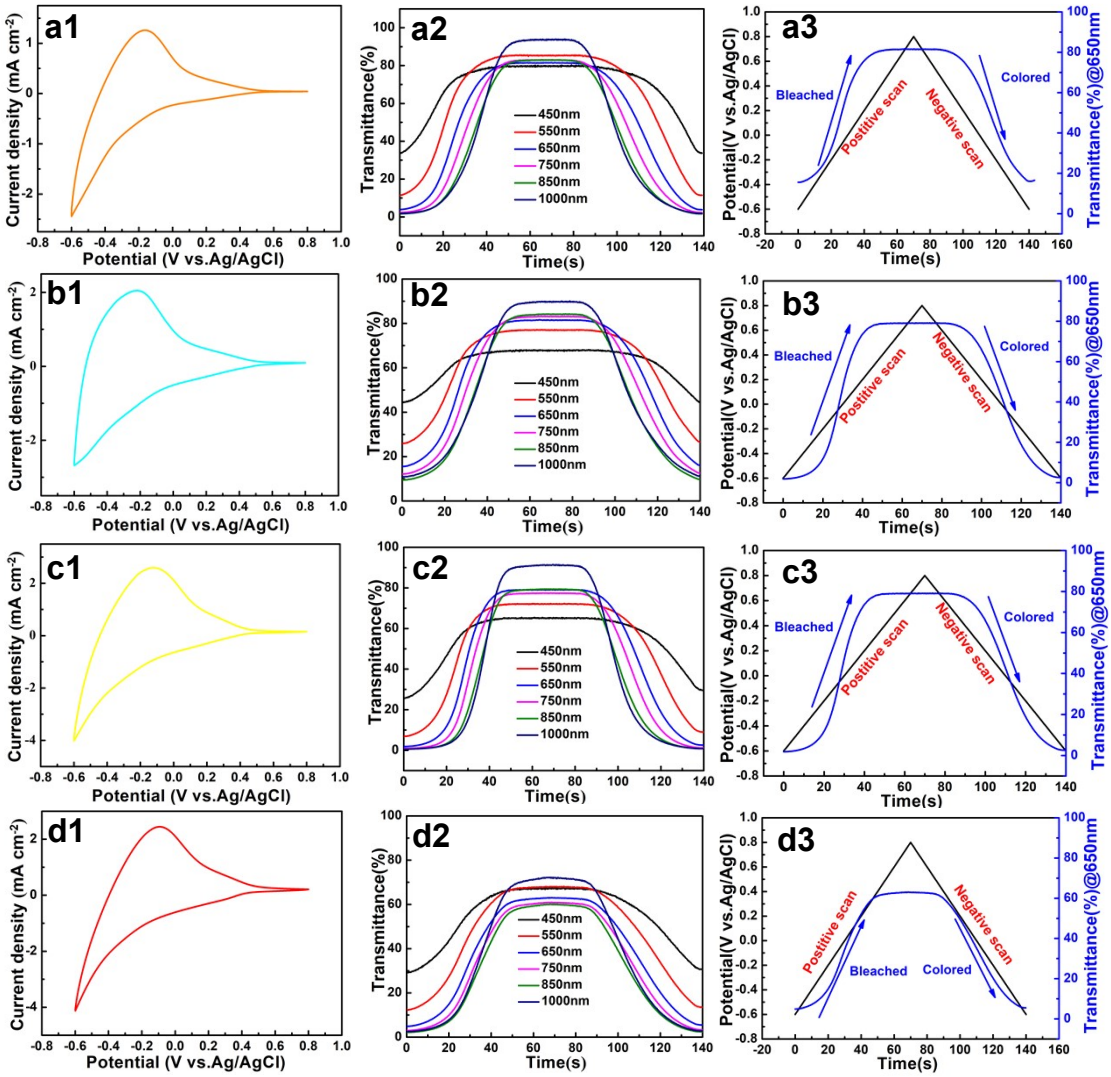

Figure S7. CV curves at 20 mV s^{-1} and in situ corresponding spectral changes of WO_3 nanosheets array/FTO dual-functional electrode: (a1, a2 and a3) WO_3 /FTO-0, (b1, b2 and b3) WO_3 NSHs/FTO-0.4, (c1, c2 and c3) WO_3 NSHs/FTO, (d1, d2 and d3) WO_3 NSHs/FTO-0.6.

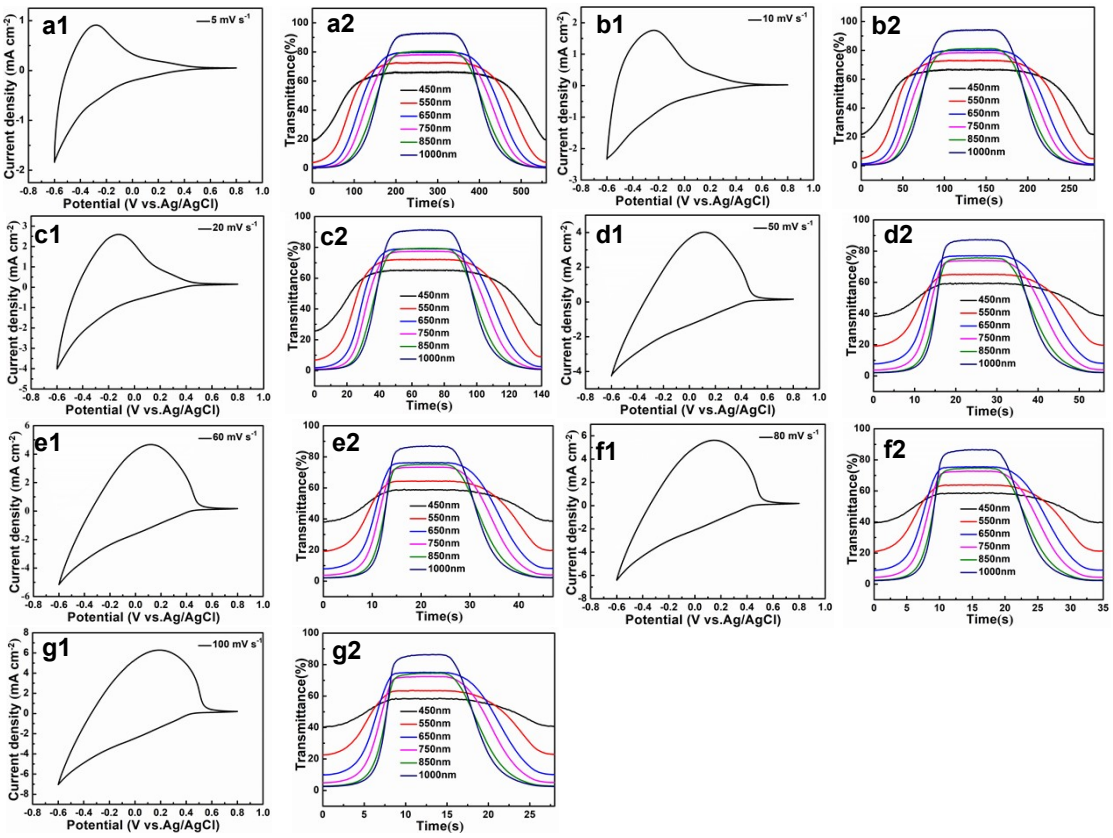

Figure S8. CV curves and in situ corresponding spectral changes of WO_3 nanosheets array/FTO dual-functional electrode at different scan rates: (a1 and a2) 5 mV s^{-1}, (b1 and b2) 10 mV s^{-1}, (c1 and c2) 20 mV s^{-1}, (d1 and d2) 50 mV s^{-1}, (e1 and e2) 60 mV s^{-1}, (f1 and f2) 80 mV s^{-1}, (g1 and g2) 100 mV s^{-1}.

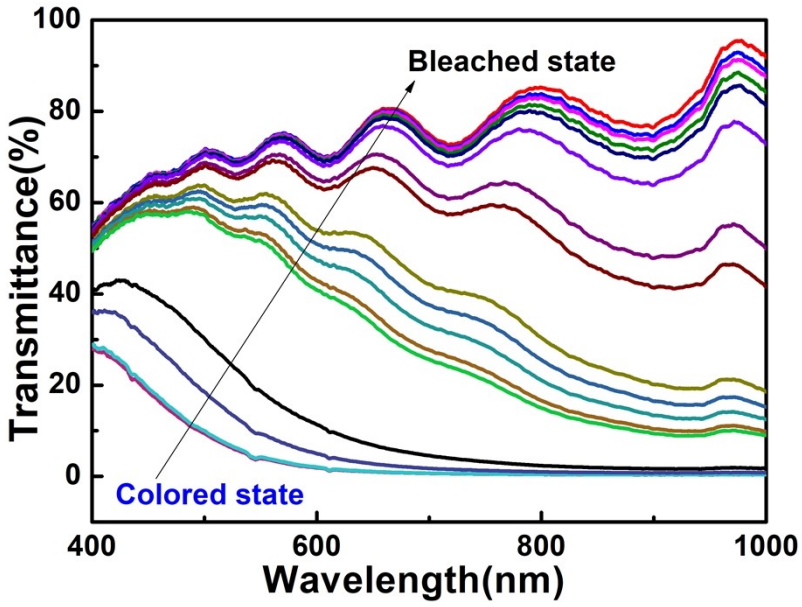

Figure S9. Full transmittance spectra of the WO_3 nanosheets array/FTO electrode during the positive scan of 5 mV s^{-1}.

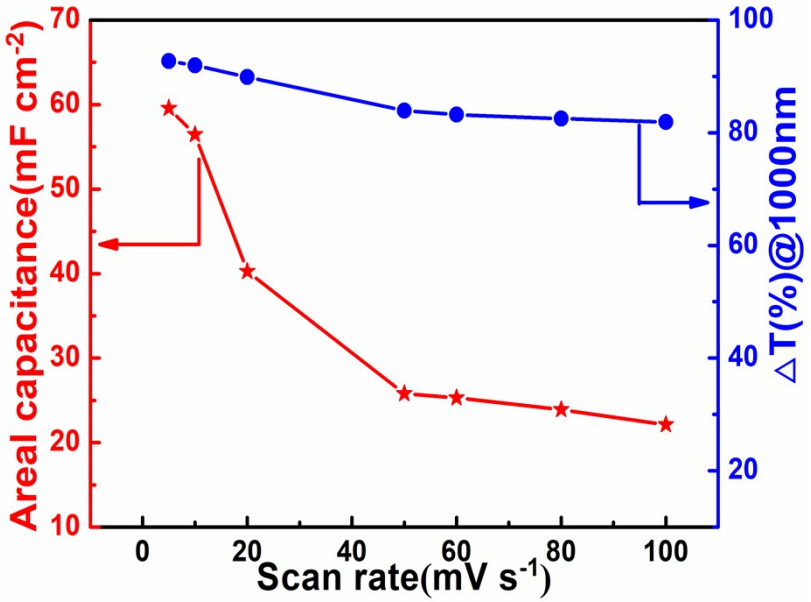

Figure S10. Areal specific capacitance and corresponding optical modulation at 1000 nm at different scan rates.

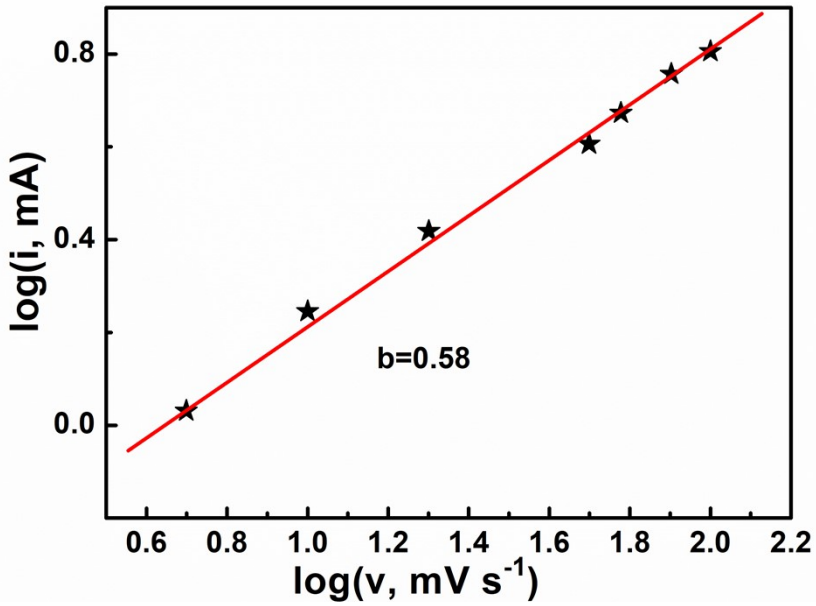

Figure S11. The determination of the b-value at anodic peak regimes.

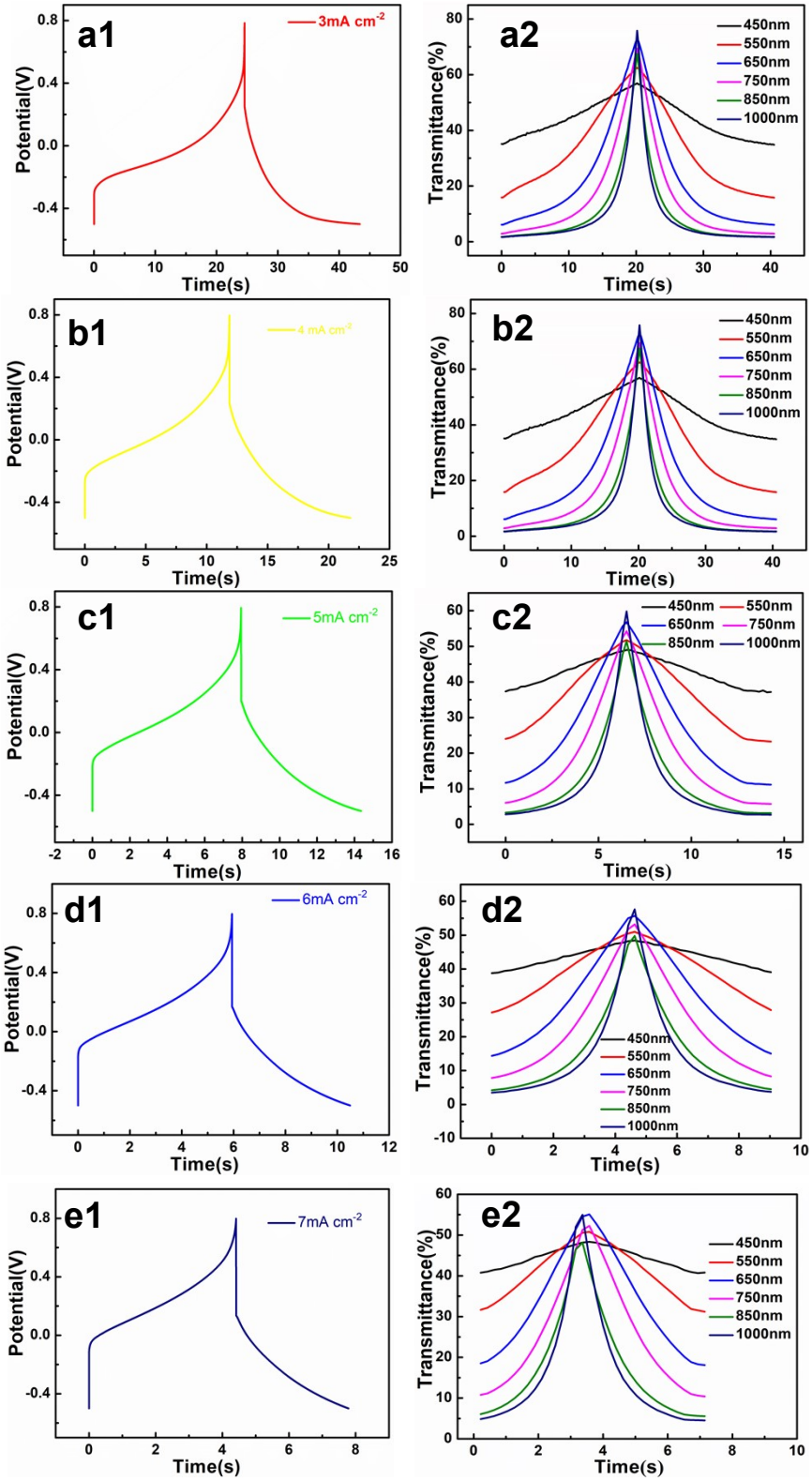

Figure S12. The CP curves and in situ corresponding spectral changes for the WO_3 nanosheets array/FTO electrode at different current densities: (a1 and a2) 3 mA cm^{-2}, (b1 and b2) 4 mA cm^{-2}, (c1 and c2) 5mA cm^{-2}, (d1 and d2) 6 mA cm^{-2}, (e1 and e2) 7 mA cm^{-2}.

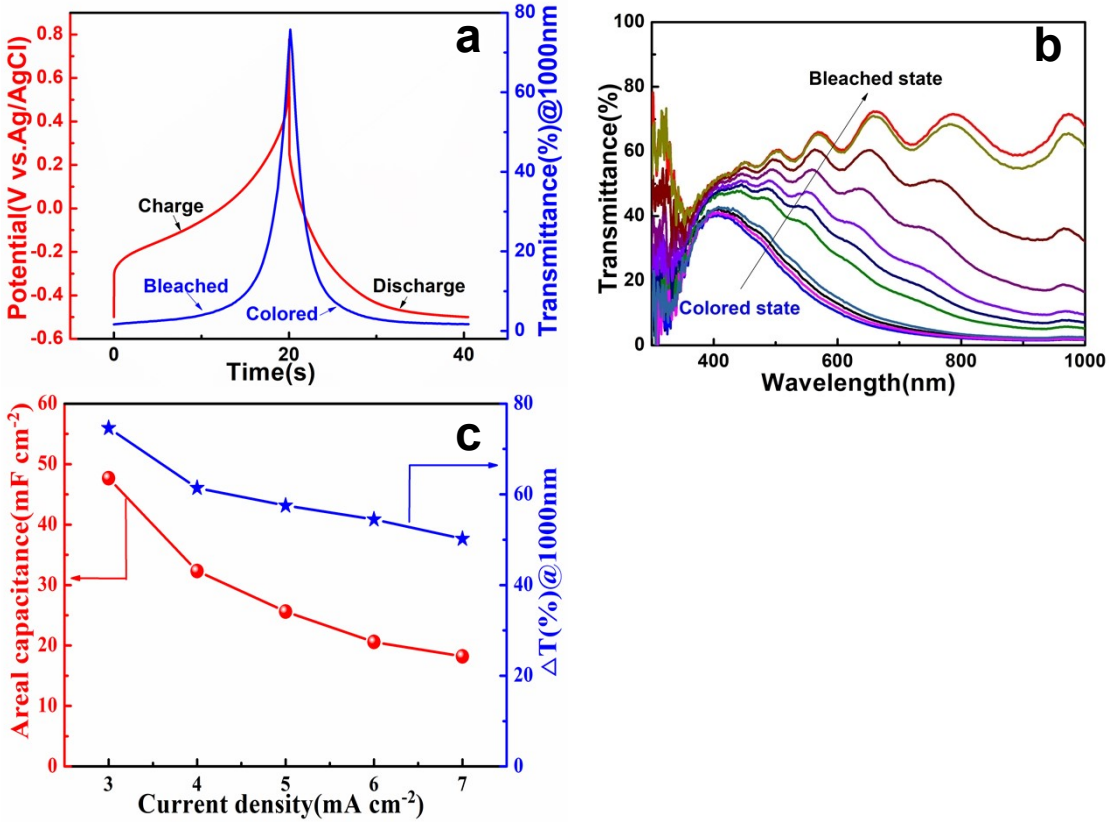

Figure S13. (a) The relationship between transmittance change profile at 1000 nm and charge/discharge curve at 3 mA cm^{-2}, (b) Full transmittance spectra of the WO_3 nanosheets array/FTO electrode during the charge process at 3 mA cm^{-2}, (c) Influence of different current densities on the areal specific capacitance and the transmittance change at 1000 nm of the WO_3 NSHs/FTOelectrode.

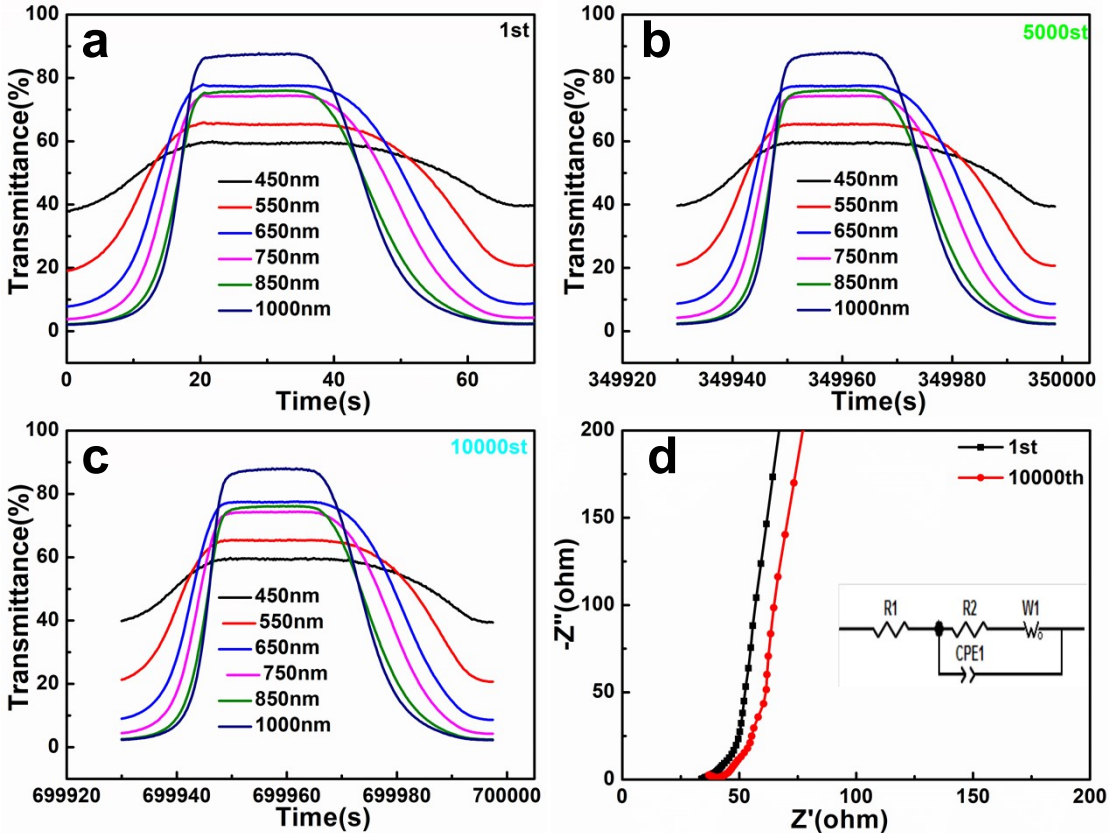

Figure S14. (a), (b) and (c) In-situ corresponding spectral changes at a scan rate of 40 mV s^{-1} after different CV cycles, (d) Nyquist plots of the WO_3 nanosheets array/FTO electrode before and after 10000 cycles.

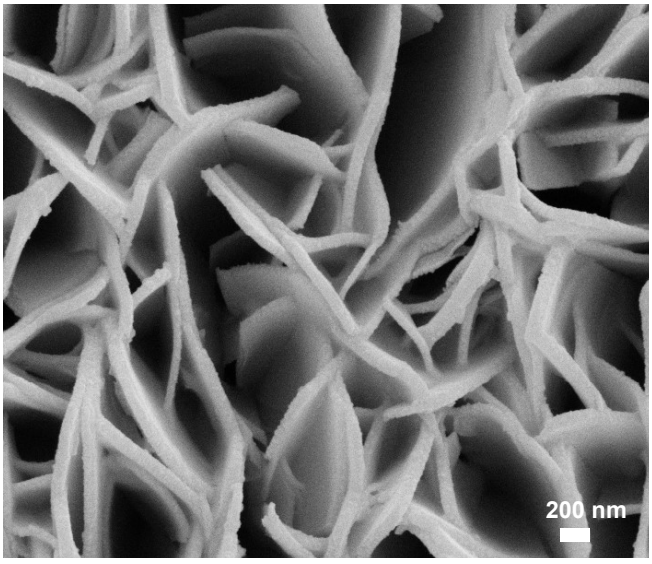

Figure S15. SEM images of the WO_3 nanosheets array/FTO electrode after 10000 cycles.

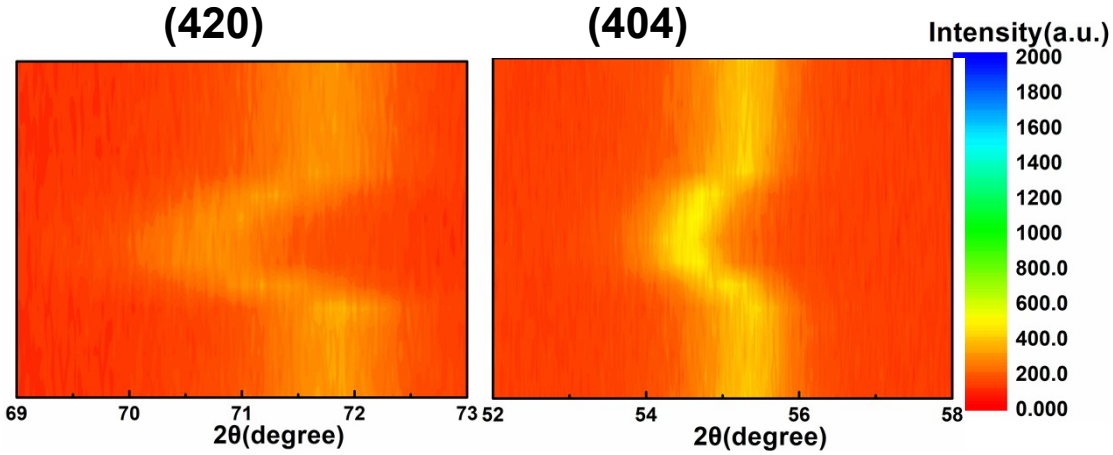

Figure S16. The corresponding 2D contour maps of (420) and (404) peaks of WO_3 nanosheets array/FTO electrode.

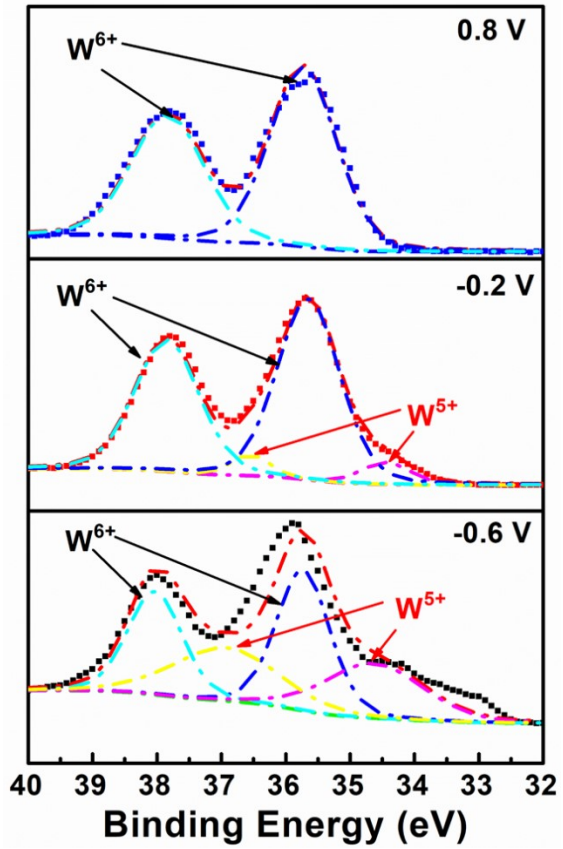

Figure S17. Ex-situ XPS spectra of W 4f at different potential states of WO_3 nanosheets array/FTO electrode.

Table S1 Comparison of the electrochromic and energy storage performance between WO_3 in this work and before.

Samples	Optical modulation	Areal capacitance	Cycle life	Reference
WO_3/ZnO nanowire array	41.5 % (0.14 mA cm^{-2})	7.13 mF cm^{-2} (0.14 mA cm^{-2})		43
P5FIn/WO_3	46 % (0.1 mA cm^{-2})	34.1 mF cm^{-2} (0.1 mA cm^{-2})	93% (5000 cycles)	44
amorphous/crystalli-ne WO_3 nanoporous arrays	80% (0.14 mA cm^{-2})	35.2 mF cm^{-2} (1.12 mA cm^{-2})	84% (2000 cycles)	45
h-WO_3/TiO_2 nanorods array	73.45% (-1 V and 1.0 V)	10.93 mF cm^{-2} (0.14mA cm^{-2})	92.9% (2000 cycles)	46
porous amorphous WO_3 nanostructures	83 % (0.14 mA cm^{-2})	35.12 mF cm^{-2} (1.12 mA cm^{-2})	95.7% (2000 cycles)	47
cauliflower-like WO_3	65% (-0.6 V and 0 V)	45 mF cm^{-2} (2 mA cm^{-2})		48
WO_3 nanoplates	55% (-0.6 V and 0.6 V)	72.6 mF cm^{-2} (0.2 mA cm^{-2})		4
WO_3 nanosheets	56.7 % (0.11 mA cm^{-2})	14.9 mF cm^{-2} (0.11 mA cm^{-2})		49
	74.62 % at 1000 nm (3 mA cm^{-2})		89.29% capacity retention ratio (10000 cycles)	
WO_3 nannoshees array/FTO	60.89 % at 633nm (3 mA cm^{-2})	47.65 mF cm^{-2} (3 mA cm^{-2})	93.4% optical modulation retention ratio (10000 cycles)	this work

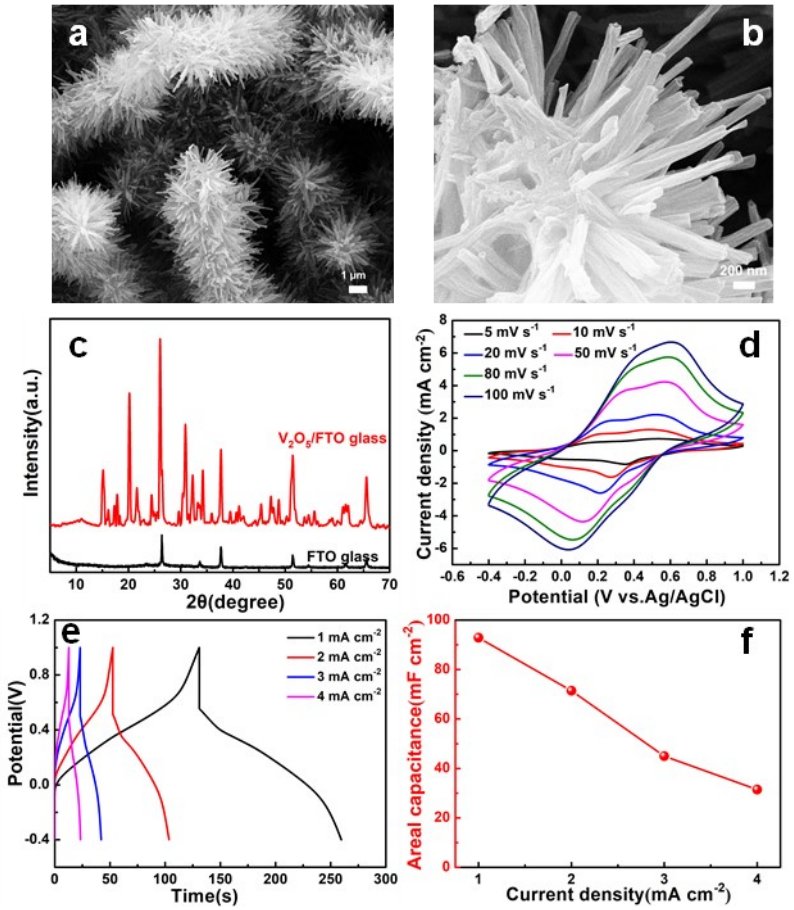

Figure S18. (a) and (b) SEM images, (c) XRD pattern of the V_2O_5 /FTO, (d) CV curves of the electrode at different scan rates, (e) CP curves of full cell at different current densities from 1 to 4 mA cm^{-2}, (f) The areal specific capacitance at different scan rates.

As shown in Figure S18a and b, the SEM images show that the holothurian-like V_2O_5 material with average diameters of 1.5 ± 0.6 μm consist of individual nanotubes connected to a central core. In Figure S18c, XRD pattern of V_2O_5/FTO can be indexed to orthorhombic V_2O_5 (JCPDS card no. 76-1803) with Pmn 21 space group. The electrochemical performance of the V_2O_5/FTO was evaluated by CV and CP tests. All the CV curves (Figure S18d) show obvious redox peaks, which indicates that typical Faraday pseudocapacitance behavior occurs in the energy storage process. As shown in Figure S18e, the nonlinear behavior of all CP curves reveals the pseudocapacitive nature of V_2O_5/FTO electrode, which is consistent with the CV results. The specific capacitance of the V_2O_5/FTO electrode can be calculated based on the discharge curves in Figure S18e and the results are plotted in Figure S18f. The specific capacitances of the electrode at 1, 2, 3 and 4 mA cm^{-2} are 92.85, 71.42, 45,

and 31.43 mF cm^{-2}, respectively.

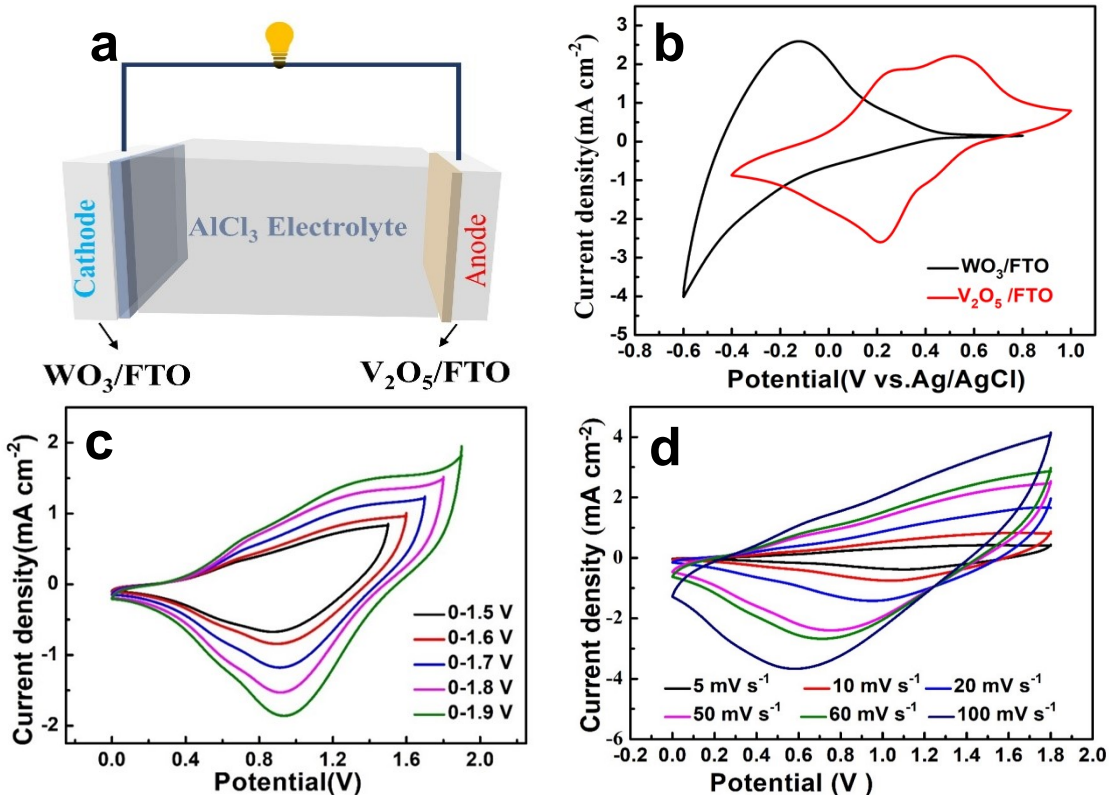

Figure S19. (a) Schematic illustration of the assembly of an electrochromic supercapacitor, (b) CV curves of WO_3 nanosheets array/FTO and V_2O_5 /FTO electrode tested in three-electrode system at the scan rate of 20 mV s^{-1}, (c) CV curves of the ESC device at different potential windows during the scan rate of 20 mV s^{-1}, (d) CV curves of the device at different scan rates.

Table S2. The digital photos of the electrochromic supercapacitor at different capacity status and corresponding (L a b) values.

Areal specific capacitance (mF cm^{-2})	Digital photos	L	a	b
26.11		7	-1	-13
24.37		10	-2	-13
17.83		23	-6	-19
10.00		47	-6	-4
1.87		59	-4	2
0		75	-1	5

References

S1. M. Qiu, P. Sun, L. Shen, K. Wang, S. Song, X. Yu, S. Tan, C. Zhao and W. Mai, *J. Mater. Chem. A*, 2016, **4**, 7266-7273.

S2. C. Yao, B. Wei, H. Li, G. Wang, Q. Han, H. Ma and Q. Gong, *J. Mater. Chem. A*, 2017, **5**, 56-61.

S3. B. R. Koo, M. H. Jo, K. H. Kim and H. J. Ahn, *NPG Asia Mater.*, 2020, **12**, 1-12.

S4. K. A. Owusu, L. Qu, J. Li, Z. Wang, K. Zhao, C. Yang, K. M. Hercule, C. Lin, C. Shi, Q. Wei, L. Zhou and L. Mai, *Nat. Commun.*, 2017, **8**, 1-11.

S5. D. Mandal, P. Routh and A. K. Nandi, *Small*, 2018, **14**, 1702881.

S6. S. Wang, H. Xu, T. Hao, P. Wang, X. Zhang, H. Zhang, J. Xue, J. Zhao and Y. Li, *NPG Asia Mater.*, 2021, **13**, 1-11.

S7. Y. Liang, Y. Yang, C. Zou, K. Xu, X. Luo, T. Luo, J. Li, Q. Yang, P. Shi and C. Yuan, *J. Alloys Compd.*, 2019, **783**, 848-854.

S8. R. Dong and J. Hao, *Chem. Rev.*, 2010, **110**, 4978-5022.